

Revision3

Quantitative determination of the shock stage of L6 ordinary chondrites using X-ray diffraction

NAOYA IMAE^{1,2,*} AND MAKOTO KIMURA^{1,**}

¹National Institute of Polar Research, 10-3 Midori-cho, Tachikawa-shi, Tokyo 190-8518, Japan

²SOKENDAI, 10-3 Midori-cho, Tachikawa-shi, Tokyo 190-8518, Japan

Corresponding author: Naoya Imae

* E-mail: imae@nipr.ac.jp

** E-mail: kimura.makoto@nipr.ac.jp

Submitted to American Mineralogist

Manuscript#7554

9 April 2020

Revised 10 September 2020

Revised 9 October 2020

ABSTRACT

The shock stages of 14 L6 ordinary chondrites are estimated using the random X-ray diffraction patterns of polished thin section samples and the in-plane rotation method. The mean lattice strains and grain size factors for olivine and orthopyroxene are determined from the analyses based on the Williamson-Hall plots, which depict the tangent Bragg angle and integral breadth β . The lattice strain in olivine, ε^{Ol} , is distributed from $\sim 0.05\%$ to $\sim 0.25\%$, while that in orthopyroxene, ε^{Opx} , is distributed from $\sim 0.1\%$ to $\sim 0.4\%$, where we selected the isolated peaks of olivine and orthopyroxene. The olivine peaks have Miller indices of (130), (211), (222), (322), while the orthopyroxene peaks have Miller indices of (610), (511), (421), (631), (12.1.2). The intercept for integral breadth β_0^{Ol} and β_0^{Opx} for the Williamson-Hall plots correlates with the grain size of the constituent minerals. The grain size is proportional to the inverse of β_0 since the β intercept increases with the shock stage. Introducing a new parameter, $-\varepsilon/\log \beta_0$ for olivine (0.04–0.16) and orthopyroxene (0.07–0.32) reveals a clear relationship between them: $-\varepsilon^{Opx}/\log \beta_0^{Opx} = -0.01 + 2.0 (-\varepsilon^{Ol}/\log \beta_0^{Ol})$ ($R > 0.9$). In addition, the isolated peak of plagioclase ($\bar{2}01$) systematically changes as the shock stage increases, suggesting the progress of amorphization (maskelynitization). Another parameter, $(I/FWHM)_{Pl(\bar{2}01)}$, reveals additional relationships: $-\varepsilon^{Ol}/\log \beta_0^{Ol} = 0.14(\pm 0.01) - 5.2 \times 10^{-5}(\pm 5.7 \times 10^{-6}) \times (I/FWHM)_{Pl(\bar{2}01)}$, and $-\varepsilon^{Opx}/\log \beta_0^{Opx} = 0.25(\pm 0.04) - 8.9 \times 10^{-5}(\pm 2.6 \times 10^{-5}) \times 10^{-5} \times (I/FWHM)_{Pl(\bar{2}01)}$. These three parameters systematically change with the shock stage, suggesting that they are suitable shock barometers. The present method is useful to evaluate the shock stage of L6 chondrites and potentially enables quantitative shock stage classification for stony meteorites.

Keywords: Olivine, orthopyroxene, ordinary chondrites, X-ray diffraction, lattice strain, shock metamorphism

INTRODUCTION

Laboratory X-ray diffraction (XRD) methods are useful tools to characterize extraterrestrial materials. Some studies have macroscopically examined powder samples (e.g., Howard et al. 2009; Howard et al. 2010; Dunn et al. 2010) and polished thin sections (Imae and Nakamuta 2018; Imae et al. 2019), while others have microscopically investigated submillimeter grains (Imae and Kimura 2020) and $\sim 50 \mu\text{m}$ -sized grains (Uchizono et al. 1999; Nakamuta and

Motomura 1999; Nakamura et al. 2001; Nakamuta et al. 2006; Flemming et al. 2007; Jenkins et al. 2019). These approaches can identify the constituent phases, their chemical composition (e.g., Mg-Fe in olivine), the shock stage, the shock metamorphism (Uchizono et al. 1999; Jenkins et al. 2019; Imae et al. 2019), and thermal metamorphism (Imae and Nakamuta 2018; Imae et al., 2019) as well as determine the modal abundance of the constituent minerals (Howard et al. 2009; Dunn et al. 2010).

Stöffler et al. (1991) established a shock stage classification of ordinary chondrites by textural observations and shock recovery experimental results. The results are defined on a scale of S1 to S6, where the shock peak pressure increases from S1 (<~3 GPa) to S6 (>~50 GPa). The classification of the degree of shock in chondrites is somewhat descriptive (Stöffler et al. 1991; Stöffler et al. 2018; Schmitt 2000). Chondrites exhibit diverse shock effects, which can be observed under an optical microscope, such as undulatory extinction, mosaic texture, planar deformation feature (PDF), brecciation, shock melt vein formation, recrystallization, and annealing after shock (Stöffler et al. 1991; Stöffler et al. 2018). However, a quantitative analytical technique to measure shock effects on ordinary chondrites has yet to be established.

Crystal defects such as dislocations, which originate from subgrain or subdomain microorientations, form both undulatory extinctions and mosaic textures. Undulatory extinctions are correlated with the lattice strain due to the deviation of the unit cell, and are detected as broadening of the XRD diffraction peaks. In contrast, mosaic textures are due the organization of dislocations into discrete arrays, and are detected as a grain size factor under XRD as a function of the tangent of the Bragg angle. Additionally, they may be detected as dislocation densities under a transmission electron microscope (TEM). Jenkins et al. (2019) identified the mosaic texture by a streak of the Laue spot along the Debye ring (strain-related mosaicity) using a two-dimensional (2D) detector.

Among the shock effects in extraterrestrial materials, strain can be evaluated using macroscopic X-ray diffractions. Imae et al. (2019) recently found that the full width at half maximum (FWHM) of the olivine (Ol) (130) lattice plane measured in 11 L6 chondrites show a positive correlation with the shock stages (S1–S5) defined by Stöffler et al. (1991; 2018; 2019). However, the relationship for the FWHM of the diffraction peaks from orthopyroxene is less distinct than that of olivine (Imae et al. 2019). The FWHM is correlated with the lattice strain that

formed during the shock processes, and can be observed as diffraction line broadening. However, these works did not consider the strain-related mosaicity.

Lattice strain in minerals (mainly silicates) is an essential parameter for quantifying the shock effects of stony meteorites. The mean lattice strain in the main constituent minerals, olivine and orthopyroxene, is a primary parameter to quantify the degree of shock metamorphism in stony meteorites (e.g., Uchizono et al. 1999; Imae 2019). Uchizono et al. (1999) experimentally determined the relationship between strain in olivine and shock pressure. The strain in olivine can be obtained from the Williamson-Hall plot (e.g., Uchizono et al. 1999). Nakamuta et al. (2006) found the maximum lattice strain of olivine using eight equilibrated ordinary chondrites (2 H6, 1 L5, 2 L6, 1 LL6, and 1 LL melt) and a Gandolfi camera. They estimated the shock pressures using the calibration curve by Uchizono et al. (1999) and defined the shock stage quantitatively.

Recently, Jenkins et al. (2019) estimated the shock pressure from olivine in Martian meteorites using the calibration curve by Uchizono et al. (1999). Additionally, they applied the Williamson-Hall plot to olivine in Martian meteorites and derived the lattice strain to evaluate the degree of shock metamorphism. Finally, they analyzed the shock history using the strain-related mosaicity and integral breadth.

Flemming (2007) proposed a method using a 2D detector. The strain related mosaicity is an important parameter related to the grain destruction process (grain size distribution) as it evaluates the shock effect and strain, especially since the shock effect appears as mosaicism of grains and PDFs. However, Uchizono et al. (1999) and Imae et al. (2019) did not consider the grain mosaicity. Our research takes into account the grain mosaicity effect using another analytical approach.

In the present study, the X-ray diffraction data of 14 L6 ordinary chondrites were obtained by the in-plane rotation method applied to polished thin sections (PTS). Then the diffraction data was analyzed with Williamson-Hall plots using the isolated indices for olivine and orthopyroxene. The mean lattice strains and crystallite sizes of olivine and orthopyroxene were obtained via the least squares method for the L6 chondrites. A new analytical technique using two parameters for lattice strains and grain size factor appears suitable to quantitatively classify the shock stage of stony meteorites. Since maskelynitization of plagioclase is another indicator to estimate the degree of shock metamorphic overprint on chondrites, we also compared it with the lattice strain-size analyses of olivine and orthopyroxene.

EXPERIMENTS AND SHOCK CLASSIFICATION

Method and samples

Using the in-plane rotation method for sectioned sample by X-ray diffractometry (SmartLab, Rigaku) at the National Institute of Polar Research (Imae and Nakamuta 2018; Imae et al. 2019), nearly random diffraction patterns of the PTSs for 14 L6 chondrites (nine Antarctic and five non-Antarctic meteorites) (Table 1) were acquired under the conditions of a scanned twofold Bragg angle (2θ) in the range of 3–75° and a length limiting slit of 5 mm with the divergence angle of (1/6)°. The samples had surface areas ~0.6–2 cm² (Table 1). L6 chondrites consisted of equilibrated mineral assemblages mainly of olivine (Fa~25), orthopyroxene (Fs~22), kamacite, and troilite, where olivine occupied 40 vol% and orthopyroxene 25 vol%. The irradiation area on the sample surface during the in-plane rotation was ~40 mm² at 20°, ~30 mm² at 30°, and 25 mm² at 40°. Thus, the irradiation area was slightly smaller than the surface area of each PTS (Table 1). Cu K_α X-ray was used under the conditions of 40 kV and 40 mA using a ceramic X-ray tube. Cu K_β was removed by the Ni filter. The Bragg–Brentano optics and a one-dimensional silicon semiconductor detector (D/tex Ultra 250) were used. The sample was rotated at a rate of 100 revolutions per minute (rpm) around the sample center during the measurements.

The samples were typically unbrecciated, consisting of a single lithology without any significant shock melt. However shock melt veins, including high-pressure polymorphs (Table 1; Fig. 1), were locally observed in several chondrites. This is similar to previous reports for Tenham (e.g., Tomioka and Miyahara 2017) and NWA 4719 (e.g., Kimura et al. 2007). High-pressure polymorphs were also reported from Sahara 98222 (wadsleyite and jadeite, Ozawa et al. 2009; Fudge et al. 2015) and Mangui (jadeite and majorite, Ji et al. 2019). The shock stage of the NWA 4719 was reclassified as S5 because recent studies suggest that S6 rarely occurs (Bischoff et al. 2019; Stöffler et al. 2019; Fritz et al. 2017). Similarly, Tenham was reclassified as S5, although S4 has been proposed for Tenham (Fritz et al. 2017; Bischoff et al. 2019). These differences are discussed later.

The following procedures were carried out to determine the indices of olivine (Ol) (space group *Pbnm*) and orthopyroxene (Opx) (space group *Pbca*) used for the Williamson-Hall plots. To avoid the effects from the resin and quartz glass contributing to the broad peak ~20°, the isolated peaks of > 30° for olivine and orthopyroxene were selected. The resin had a higher intensity than

that of the quartz glass. Other criteria for peak selection were that (1) the peak is common in all 14 L6 chondrites, and (2) the selected region spreads over the full 2θ . There were four olivine peaks with Miller indices of (130), (211), (222), and (322). Orthopyroxene had five peaks with indices of (610), (511), (421), (631), and (12.1.2). The notation of the index (12.1.2) for orthopyroxene is from Woolfson (1979). The height of Opx (610) overlapped with that of Ca-px ($\bar{3}11$), the relative intensity of Ca-px ($\bar{3}11$) was low, and the modal abundance of Ca-px in the L6 chondrites was small. Thus, the Opx (610) peak is useful in the present analyses.

To plot the tangent of Bragg angle and the integral breadth in the Williamson-Hall diagram (Williamson and Hall 1953), the profile fittings were carefully carried out using the software of PDXL (Rigaku). The Williamson-Hall plot (Williamson and Hall 1953) is given by a combination between the tangent of the Bragg angle, $\tan \theta$, for the focused indices as the horizontal axis and the integral breadths β (in the range of more than zero and much less than one degree) as the vertical axis. The equation is $\beta = \frac{\lambda}{L \cos \theta} + 4\varepsilon \tan \theta + \beta_0$ (Uchizono et al. 1999), where L is the average crystal size, β_0 is the size effect of the grains (Wilson 1962; Uchizono et al. 1999). $\frac{\lambda}{L \cos \theta}$ is negligible when the grain size is $> 1 \mu\text{m}$ (Uchizono et al. 1999), which is satisfied in this case. β includes the instrumental integral breadth as β is the integral breadth (degree unit) defined as I/h , where I is the integrated intensity of the peak and h is the peak height. β_0 is the β intercept (β at $\tan \theta = 0$), and ε is the lattice strain (Williamson and Hall 1953; Wilson 1962). $\varepsilon(\%)$ is in radian unit calculated using the factor of $100 \times (\pi/180)$. The equation shows the relation between the integral breadth and the strain derived from the Bragg equation (e.g., Wilson 1962).

The following PDF data files from the International Centre for Diffraction Data (ICDD) were used for the analyses: troilite 01-075-8712, kamacite 03-065-7752, taenite 01-071-8325, orthopyroxene 01-071-1162, 00-019-0605, and 00-007-0216, clinopyroxene 01-076-0525, forsterite 01-088-1993, diopside 01-086-0932, plagioclase 00-041-1480. In addition, various powders were prepared, and the obtained XRD patterns were used for comparison. These included synthetic forsterite (Takei and Kobayashi 1974), magnesian olivine (San Carlos, USA), orthopyroxenes (Bamble, Norway; Mpwapwa, Tanzania; the Bilanga diogenite meteorite), troilite (nodule in Nantan iron meteorite), iron (99.998%, 60 mesh, nacalai tesque), and diopside (Sar-e Sang, Afghanistan). PDXL software was used for peak profile fitting to reduce the peak intensity, integral breadth, and FWHM for the obtained peaks.

Errors (1σ) of β_0 and the slopes for olivine and orthopyroxene originating from the Williamson-Hall plots were calculated using standard statistical methods. The errors of $\log(\beta_0)$, $\varepsilon(\%)$, and $-\varepsilon/\log \beta_0$ were then calculated considering error propagation.

Shock stages of the L6 chondrites used in this study

Ordinary chondrites are classified into three major chemical groups, H, L, and LL, based on their high, low and very low concentrations of iron. L chondrites of petrologic type 6 (L6) are one of the most common type of ordinary chondrites. Hence, L6 is appropriate for this study because we can analyze samples with a wide range of shock levels, and because they are the most recrystallized and equilibrated of all L ordinary chondrites. The latter ensures that the samples are homogeneous in composition and texture, a prerequisite of applying the XRD technique used here.

Table 1 summarizes the shock stage based on the petrographic observation of the 14 L6 chondrites under an optical microscope. The classification was slightly revised from our observation (Table 1). The shock classification scheme was solely based on that of Stöffler et al. (1991), which mainly focused on undulatory extinction, mosaic texture, planar deformation features of olivine, and maskelynitization of plagioclase.

Polysynthetic twinning of clinoenstatite occurs due to rapid cooling after crystallization from the mafic silicate melt, and is commonly observed in chondrules of unequilibrated chondrites. However, polysynthetic twinning of clinoenstatites has also been observed in L6 chondrites using optical microscopy (Imae et al. 2019). Polysynthetic twinning, however, is rare and typically applies to one grain in one polished thin section of any L6 chondrite (Imae et al. 2019). A polysynthetic twinning texture may also suggest a severe shock effect before annealing (Rubin 2002; Rubin 2004; Ruzicka et al. 2015; Friedrich et al. 2017) because the phase transition of orthopyroxene to clinopyroxene under high pressure has been studied (e.g., Coe 1970; Coe and Muller 1973; Clément et al. 2018).

Complementary textural observations

Polarizing optical microscopes (BX60, Olympus and DM4000M with LAS Power Mosaic software, Leica) were used for textural observations of the polished thin sections. Using a field emission scanning electron microscope (FE-SEM: JSM-7100F, JEOL), the textures of the L6 chondrites were observed in the ~ 1 nA beam condition with an accelerating voltage of 15 kV.

Additionally, using an electron probe microanalyzer (EPMA: JXA-8200, JEOL), the compositions of the constituent phases were determined using a 9 nA beam current for olivine and pyroxene and using 3 nA beam current defocused at 5 μm beam for maskelynites, both with an accelerating voltage of 15 kV. The standards were identical with those by Imae and Ikeda (2010). Micro-Raman spectroscopy (NRS-1000, JASCO) was used under similar conditions as those used by Imae and Ikeda (2010) and Imae et al. (2019). Raman spectroscopy was used to identify maskelynite in the equigranular texture and the high-pressure polymorphs in shock melt veins for the Tenham and NWA 4719 L6 chondrites.

RESULTS

Figures 2a–2n, Figs. 2o–q, and Figs. 2r–s shows the X-ray diffraction patterns for the 14 L6 chondrites, diffractions of orthopyroxenes, and the intensity PDF data, respectively. Olivine peaks are the most abundant followed by orthopyroxene peaks. Fe–Ni alloys and troilite peaks are rare, and are mainly limited to kamacite (110) at 44.6° , taenite (111) at 43.8° , and troilite (114) at 43.1° . Although plagioclase peaks are abundant, their intensities are weak. The principal peak is limited to be $2\theta = \sim 22^\circ$ due to the low modal abundance of plagioclase.

Olivine

Figure 3a shows the Williamson-Hall plot for olivine in the 14 L6 chondrites. The horizontal axis ($\tan \theta$) is positively correlated with the vertical axis (β), indicating a good correlation factor R in the range of 0.68–1.00. In fact, $R > 0.85$ for 11 of the 14 chondrites. When the shock stage increases, the data point plot shifts upwards. The slope of the least-squares gives the lattice strain. The slope (4ε) is 0.14 for S1, 0.14–0.18 for S2, 0.16–0.42 for S3, 0.28–0.51 for S4, and 0.43–0.62 for S5. Due to the low correlation factor ($R = 0.68$), 0.10 for S3 (Y–87010) is excluded. Table 2 summarizes the obtained lattice strain, ε^{Ol} (%), with errors (1σ).

Orthopyroxene

Figure 3b shows the Williamson-Hall plot for orthopyroxene in the 14 L6 chondrites. Similar to olivine, the horizontal axis tends to show a positive correlation with the vertical axis. However, the correlation is unclear in some chondrites (Y–791771 S4 and NWA 4719 S5, Table 2 and Fig. 3b). All samples with unclear correlations are classified into high shock stages. The

Williamson-Hall plots for the other samples of orthopyroxene show a relatively good correlation factor of 0.70–0.97. The slope (4ε) is 0.2 for S1, 0.22–0.28 for S2, 0.36–0.74 for S3, 0.79–0.91 for S4, and 0.24–0.68 for S5. Thus, the strain is positively correlated with the shock stages of S1–S5. Table 2 summarizes the lattice strain, $\varepsilon^{\text{Opx}}(\%)$, which have correlation factors of $R \geq \sim 0.7$. Table 3 summarizes the analytical results of the Williamson-Hall plot with errors (1σ).

Plagioclase

The main isolated peak of plagioclase occurs at $\sim 22^\circ$ with an index of $(\bar{2}01)$ (Fig. 2). At first glance, the Opx (211) peaks overlap around 22.10° in case of PDF 01-071-1162, $I = 13.2$. However, the peak of Opx (211) from Bamble (Fig. 2o), Mpwapwa (Fig. 2p), a diogenite (Fig. 2q), PDF 00-019-0605, and PDF 00-007-0216 is much lower than that from the PDF 01-071-1162. Alternatively, the peak itself is lacking. Therefore, the peak is isolated and does not significantly overlap with peaks from other phases. There is a clear trend between FWHM and the integrated intensity (Fig. 4a). When the shock stage increases from S1 to S3, the FWHM increases. Further increasing the shock stage to S4 decreases the peak intensity as the FWHM increases. Finally, both FWHM and intensity progress towards zero in S5. The trend is consistent with maskelynitization or amorphization of plagioclase.

DISCUSSION

Relationship between lattice strain and grain size factor in olivine

The strain in olivine, $\varepsilon^{\text{Ol}}(\%)$, continuously increases from S1 to S5 shock stages, and the value ranges from ~ 0.06 up to ~ 0.27 , although the strain values among S1–S5 overlap (Tables 2 and 3). The shock process results in an increase in both the lattice strain and fracture density.

The intercept of the integral breadth, β_0 , may be another independent function of shock metamorphism. It may correspond to mechanical destruction such as mosaicism and planar deformation features (e.g., Stöffler et al. 1991). The parameters $-\log \beta_0^{\text{Ol}}$ and ε^{Ol} correlate positively for each shock stage although errors (1σ) are large (Fig. 5a). Therefore, we introduce a new parameter of $-\varepsilon^{\text{Ol}}/\log \beta_0^{\text{Ol}}$ (Table 2).

Shock may decrease the grain size. The grain size factor β_0 in Fig. 3a increases as the shock stage increases. This suggests that β_0 is inversely correlated with the grain size. Considering the

grain size changes exponentially, the logarithm of β_0 would be appropriate. However, the literature lacks detailed information about the parameter to resolve the grain size. The parameter of $-\epsilon^{Ol}/\log \beta_0^{Ol}$ shows a good correlation with the shock stage (Fig. 6a). Hence, X-ray diffraction may serve as a quantitative shock barometer. For reference, figure 6a shows the average of the peak shock pressure from Stöffler et al. (1991) and the subsequent references (e.g., Stöffler et al. 2018, 2019, Fritz et al. 2017).

Relationship between lattice strain and grain size factor of orthopyroxene

Similarly, the strain, ϵ^{Opx} (%), in orthopyroxene continuously increases from S1 to S5 shock stages. The value is from ~ 0.08 to ~ 0.4 , which is slightly higher than those of olivine. However, the strain values among S1–S5 overlap (Tables 2 and 3). The relationship between $-\log \beta_0^{Opx}$ and ϵ^{Opx} shows a correlation (Fig. 5b). Therefore, we introduce the parameter of $-\epsilon^{Opx}/\log \beta_0^{Opx}$ (Table 2). Similar to olivine, the relationship for orthopyroxene as a quantitative shock barometer is derived with a good correlation (Fig. 6b). For reference, Fig. 6b shows the average of the peak shock pressure by the shock stage.

Maskelynitization of plagioclase

The combined analyses of the intensity of plagioclase with the FWHM suggest a clockwise rotation as the shock stage increases, which is indicated as an arrow in Fig. 4a. Maskelynitization or amorphization of plagioclase is then observed as a decrease in peak intensity for FWHM as the shock stage increases (Fig. 4b). Kubo et al. (2010) experimentally showed that the amorphization of sodic plagioclase occurs in the range of 20–30 GPa, but recent experiments by Fritz et al. (2019) revised it to 25–35 GPa. The pressure range may correspond to S4, where the amount of plagioclase significantly decreases and that of maskelynite increases (Stöffler et al. 1991), which is consistent with the observation in Fig. 4.

Other influences on the relationship between lattice strain and grain size factor

Shock metamorphism induces local heating due to adiabatic shock compression during hypervelocity impact (Sharp and DeCarli 2006). The post-shock temperature may result in the local formation of a shock melt vein, recrystallization, local melting such as melt pocket, and annealing textures (Stöffler et al. 1991). These textural changes may significantly affect the

observed relationship for the shock stage between the lattice strain and the crystallite size. Local heating may play a role in reducing the slope of shock stage parameter, $-\varepsilon/\log \beta_0$, versus shock pressure as the pressure increases (Fig. 6).

High-pressure polymorphs occur in the shock melt veins from the Tenham and NWA 4719 L6 chondrites with shock stage S5 (Sharp and DeCarli 2006; Tomioka and Miyahara 2017). We identified ringwoodite in NWA 4719 (Figs. 7a, 7b, and 8a). Shock melt veins also occur from less shocked L6 chondrites of Sahara 98222 S3 (Ozawa et al. 2009; Fudge et al. 2015) and Mangui S4 (Ji et al. 2019). The constituent minerals surrounding a shock vein would also experience some degree of heating, resulting in annealing or recrystallization during the formation of shock veins. The effects of annealing and recrystallization as well as the formation of the shock melt veins may play a significant role in releasing the lattice strains of minerals, although these processes occur locally.

The local recrystallization texture appears in a limited portion from the highly shocked samples of the Tenham and NWA 4719 L6 chondrites. The texture in the NWA 4719 L6 chondrite (Fig. 7c) is characterized by a well-crystallized triple junction with an equigranular texture. The compositions for the major constituent phases of olivine, Ca-rich pyroxene, orthopyroxene, and maskelynite are identical to the mean composition for the host lithology of the NWA 4719 L6 chondrite (Fig. 7b). The texture suggests a local temperature increase during shock metamorphism. Micro-Raman spectroscopy suggests that maskelynites in the equigranular areas form assemblages at high temperatures below liquidus during shock metamorphism in Fig. 8b (e.g., Fritz et al. 2005). Consequently, heating by shock may have a relieving or resetting effect on both the lattice strain and grain size.

IMPLICATIONS

Shock metamorphism on extraterrestrial materials is important for clarifying planetary formation and evolution processes. However, the current shock classification defined by Stöffler et al. (1991) is qualitative and somewhat user subjective. Controversial shock stages have been assigned for single meteorites (e.g., Tenham previously S6). However, this study suggests an S5 shock stage, while Fritz et al. (2017) suggest S4. Our new analytical method of the shock effects on the stony meteorites is useful to quantitatively identify the shock stage. Undulatory extinction under an optical microscope indicates lattice strain. The mechanical destruction texture, mosaic

texture, and planar deformation features seen under an optical microscope correspond to the crystallite size. The lattice strain, ε^{Ol} (%), in olivine varies from $\sim 0.05\%$ to $\sim 0.25\%$ while that in orthopyroxene, ε^{Opx} , varies from $\sim 0.1\%$ to $\sim 0.4\%$, suggesting that lattice strain in orthopyroxene is more significant than that in olivine. This may imply that orthopyroxene is more susceptible to the strain than olivine or olivine tends to release the strain compared with orthopyroxene.

Introducing a new parameter, $-\varepsilon/\log \beta_0$ for olivine (0.04–0.16) and orthopyroxene (0.07–0.32) reveals clear relationships between them. $-\varepsilon^{\text{Opx}}/\log \beta_0^{\text{Opx}} = -0.01 + 2.0 (-\varepsilon^{\text{Ol}}/\log \beta_0^{\text{Ol}})$ ($R = 0.94$) (Fig. 9a). In addition, plagioclase focusing on an index of $(\bar{2}01)$ becomes amorphous (maskelynite) as the shock stage increases, using another parameter $(I/FWHM)_{Pl(\bar{2}01)}$. The ratio for plagioclase, $(I/FWHM)_{Pl(\bar{2}01)}$, is correlated with our shock barometer using olivine and orthopyroxene of ordinary chondrites (Fig. 9b and 9c). Hence, $-\varepsilon^{\text{Ol}}/\log \beta_0^{\text{Ol}} = 0.14(\pm 0.01) - 4.6 \times 10^{-5} (\pm 5.7 \times 10^{-6}) \times (I/FWHM)_{Pl(\bar{2}01)}$ (Fig. 9b), and $-\varepsilon^{\text{Opx}}/\log \beta_0^{\text{Opx}} = 0.25(\pm 0.04) - 8.9 \times 10^{-5} (\pm 2.6 \times 10^{-5}) \times (I/FWHM)_{Pl(\bar{2}01)}$ (Fig. 9c). The regression line and the error in Figs. 9a and 9b were estimated using different 1σ for each sample. These three parameters systematically change by shock stage of ordinary chondrites, suggesting they are suitable shock barometers. This may be useful to (re-)evaluate the shock stage. For example, is the shock stage of Tenham S4, S5, or S6? Does it depend on the section?

For the past two decades, the shock classification scheme of ordinary chondrites has been inconsistent for the high-pressure phase inventory of the melt veins. The proposed barometers may be able to estimate the variations of shock stages in a single meteorite. The application of our new shock barometer using XRD still needs to be evaluated for other types of meteorites besides L6 ordinary chondrites. Consequently, the proposed method may resolve the controversy surrounding the shock classification of ordinary chondrites by quantifying the degree of shock deformation in rock forming minerals.

ACKNOWLEDGMENTS AND FUNDING

We are grateful to Dr. Anner Peslier, Associate Editor, for the handling of our manuscript and the constructive review, and Drs. Roberta L. Flemming, Jörg Fritz, and Jacob A. Tielke for their constructive and thoughtful reviews. The study is partly supported by KAKENHI 17K05721 and NIPR Research Project KP-307. We are grateful to Yoshihiro Nakamuta, Naotaka Tomioka,

Masahiro Yasutake, and Rei Kanemaru for the discussions, and to Sen Hu for supplying and permission to use of the Mangui L6 chondrite fell in 1 June 2018 on Yunnan, China. The polished thin sections of the Antarctic meteorites and Tenham were on loan from NIPR.

REFERENCES CITED

- Bischoff A., Schleiting M., and Patzek M. (2019) Shock stage distribution of 2280 ordinary chondrites-Can bulk chondrites with a shock stage of S6 exist as individual rock? *Meteoritics & Planetary Science*, 54, 2189-2202.
- Clément, M., PadrónNavarta, J. A., Tommasi, A., and Mainprice, D. 2018. Non-hydrostatic field orientation inferred from orthopyroxene (*Pbca*) to low-clinoenstatite (*P2₁/c*) inversion in partially dehydrated serpentines. *American Mineralogist* 103, 993-1001.
- Coe, R.S. (1970) The thermodynamic effect of shear stress on the ortho-clino inversion in enstatite and other coherent phase transitions characterized by a finite simple shear. *Contributions to Mineralogy and Petrology*, 26, 247-264.
- Coe, R.S., and Muller, W.F. (1973) Crystallographic orientation of clinoenstatite produced by deformation of orthoenstatite. *Science*, 180, 64-66.
- Dunn, T.L., Cressey, G., McSween, H.Y.Jr., and McCoy, T.J. (2010) Analysis of ordinary chondrites using powder X-ray diffraction: 1. Modal mineral abundances. *Meteoritics & Planetary Science*, 45, 123-134.
- Flemming, R. L. (2007) Micro X-ray diffraction (μ XRD): a versatile technique for characterization of Earth and planetary materials. *Can. J. Earth Sci.* 44, 1333-1346.
- Friedrich, J., Ruzicka, A., Macke, R.J., Thostenson, J.O., Rudolph, R.A., Rivers, M.L., and Ebel, D.S. (2017) Relationships among physical properties as indicators of high temperature deformation or post-shock thermal annealing in ordinary chondrites. *Geochimica et Cosmochimica Acta*, 203, 157-174.
- Fritz J., Greshake A., and Stöffler D. (2005) Micro-Raman spectroscopy of plagioclase and maskelynite in Martian meteorites: Evidence of progressive shock metamorphism. *Antarctic Meteorite Research*, 18, 96-116.
- Fritz J., Greshake A., and Fernandes V. A. (2017) Revisiting the shock classification of meteorites. *Meteoritics & Planetary Science*, 52, 1216-1232.

- Fritz J., Assis Fernandes V., Greshake A., Holzwarth A., and Böttger U. (2019) On the formation of diaplectic glass: Shock and thermal experiments with plagioclase of different chemical compositions. *Meteoritics & Planetary Science*, 54, 1544-1547.
- Fudge, C., Hu, J., and Sharp, T.G. (2015) Crystallization of wadsleyite and ringwoodite in Sahara 98222, 00293 and 00350: Constraints on shock conditions. *Meteoritics & Planetary Science*, 50, A133.
- Howard, K.T., Benedix, G.K., Bland, P.A., and Cressey G. (2009) Modal mineralogy of CM2 chondrites by X-ray diffraction (PSD-XRD). Part 1: Total phyllosilicate abundance and the degree of aqueous alteration. *Geochimica et Cosmochimica Acta*, 73, 4576-4589.
- Howard, K.T., Benedix, G.K., Bland, P.A., and Cressey, G. (2010) Modal mineralogy of CV3 chondrites by X-ray diffraction (PSD-XRD). *Geochimica et Cosmochimica Acta*, 74, 5084-5097.
- Imae, N. and Ikeda, Y. (2010) High-pressure polymorphs of magnesian orthopyroxene from a shock vein in the Yamato-000047 lherzolitic shergottite. *Meteoritics & Planetary Science*, 45, 43–54.
- Imae, N. and Nakamuta, Y. (2018) A new mineralogical approach for CO3 chondrite characterization by X-ray diffraction: Identification of primordial phases and thermal history. *Meteoritics & Planetary Science*, 53, 232-248.
- Imae, N., Kimura, M., Yamaguchi, A., and Kojima, H. (2019) Primordial, thermal, and shock features of ordinary chondrites: Emulating bulk X-ray diffraction using in-plane rotation of polished thin section. *Meteoritics & Planetary Science*, 54, 919-937.
- Imae, N. and Kimura, M. (2020) New measurement technique for characterizing small extraterrestrial materials by X-ray diffraction using the Gandolfi attachment. *Meteoritics & Planetary Science* (early view).
- Jenkins, L.E., Flemming, R.L., and McCausland, P.A. (2019) Quantitative in situ XRD measurement of shock metamorphism in Martian meteorites using lattice strain and strain-related mosaicity in olivine. *Meteoritics & Planetary Science*, 54, 902-918.
- Ji, J.L., Hu, S., Kin, Y.T., Zhou, Q., Xiao, Y., Imae, N., and Kimura, M. (2019) Shock metamorphism of the new fall ordinary chondrite Mangui in China. *Meteoritics & Planetary Science*, 54, A186.

- Kimura, M., Fukuda, H., Mikouchi, T., Suzuki, A., and Ohtani, E. (2007) Abundant (Mg,Fe)SiO₃ glass in shock veins in an L6 chondrite, NWA 4719. *Meteoritics & Planetary Science*, 42, A82.
- Kubo, T., Kimura, M., Kato, T., Nishi, M., Tominaga, A., Kikegawa, T., and Funakoshi, K. (2010) Plagioclase breakdown as an indicator for shock conditions of meteorites. *Nature Geoscience*, 3, 41-45.
- Nakamura, T., Noguchi, T., Yada, T., Nakamura, Y., and Takaoka, N. (2001) Bulk mineralogy of individual micrometeorites determined by X-ray diffraction analysis and transmission electron microscopy, *Geochimica et Cosmochimica Acta*, 65, 4385-4397.
- Nakamura, Y., and Motomura, Y. (1999) Sodic plagioclase thermometry of type 6 ordinary chondrites: Implications for the thermal histories of parent bodies. *Meteoritics & Planetary Science*, 34, 763-772.
- Nakamura, Y., Yamada, S., and Yoshida, K. (2006) Estimation of shock pressure experienced by each ordinary chondrite with an X-ray diffraction method, *Meteoritical Society. Meteoritics & Planetary Science*, 41, A128.
- Ozawa, S., Ohtani, E., Miyahara, M., Suzuki, A., Kimura, M., and Ito, Y. (2009) Transformation textures, mechanisms of formation of high-pressure minerals in shock melt veins of L6 chondrites, and pressure-temperature conditions of the shock events. *Meteoritics & Planetary Science*, 44, 1771-1786.
- Rubin, A.E. (2002) Post-shock annealing of Miller Range 99301 (LL6): Implications for impact heating of ordinary chondrites. *Geochimica et Cosmochimica Acta*, 66, 3327-3337.
- Rubin, A.E. (2004) Postshock annealing and postannealing shock in equilibrated ordinary chondrites: Implications for the thermal and shock histories of chondritic asteroids. *Geochimica et Cosmochimica Acta*, 68, 673-689.
- Ruzicka, A., Hugo, R., and Hutson, M. (2015) Deformation and thermal histories of ordinary chondrites: Evidence for post-deformation annealing and syn-metamorphic shock. *Geochimica et Cosmochimica Acta*, 163, 219-233.
- Schmitt, R.T. (2000) Shock experiments with the H6 chondrite Kernoué: Pressure calibration of microscopic effects. *Meteoritics & Planetary Science*, 35, 545-560.
- Sharp, T.G., and DeCarli, P.S. (2006) Shock effects in meteorites. In D.S. Lauretta and H.Y. McSween, Eds., *Meteorites and the Early Solar System II*, p. 653-677. The University of Arizona Press, USA.

- Stöffler, D., Keil, K., and Scott, E.R.D. (1991) Shock metamorphism of ordinary chondrites. *Geochimica et Cosmochimica Acta*, 55, 3845-3867.
- Stöffler, D., Hamann, C., and Metzler, K. (2018) Shock metamorphism of planetary silicate rocks and sediments: Proposal for an updated classification system. *Meteoritics & Planetary Science*, 53, 5-49.
- Stöffler, D., Hamann, C., and Metzler, K. (2019) Addendum to "Shock metamorphism of planetary silicate rocks and sediments: Proposal for an updated classification system". *Meteoritics & Planetary Science*, 54, 946-949.
- Takei, H. and Kobayashi, T. (1974) Growth and properties of Mg_2SiO_4 single crystals. *Journal of Crystal Growth*, 23, 121-124.
- Tomioka, N., and Miyahara, M. (2017) High-pressure minerals in shocked meteorites. *Meteoritics & Planetary Science*, 52, 2017-2039.
- Uchizono, A., Shinno, I., Nakamuta, Y., Nakamura, T., and Sekine, T. (1999) Characterization of artificially shocked forsterites: (1) Diffraction profile analysis by Gandolfi camera. *Mineralogical Journal*, 21, 15-23.
- Williamson, G.K. and Hall, W.H. (1953) X-ray line broadening from filed aluminium and wolfram. *Acta Metallurgica*, 1, 22-31.
- Wilson, A.J.C. (1962) *X-ray Optics*. 127 p. John Wiley & Sons Ins., New York.
- Woolfson M. M. (1979) *An introduction to X-ray crystallography*. Cambridge University Press. 380 pp.

FIGURE CAPTIONS

FIGURE 1. Photomicrographs of the 14 polished thin sections under an optical microscope with transmitted light (Power Mosaic, Leica). Each is open nicol (plane-polarized light) and cross nicol (cross-polarized light). **(a)** A-881806 (,121–1) S1. **(b)** Y-74035 (,96–3) S2. **(c)** Y-793569 (,61–1) S2. PTS is divided into two portions, where the arrow shows the measured portion. **(d)** A-87010 (,91–1) S3. **(e)** Y-86010 (,51-1) S3. **(f)** Y-86007 (,51–1) S3. **(g)** ALH-769 (,98–2) S3. **(h)** A-881091 (,31–1) S3. **(i)** Sahara 98222 S3. **(j)** Mangui S4. **(k)** Y-791771 (,51–1) S4. **(l)** NWA 7984 S4. **(m)** Tenham (,51–3) S5. **(n)** NWA 4719 S5. The arrow shows the shock vein portion in Figs. 7a and 7b.

FIGURE 2. **(a)–(n)** X-ray diffraction patterns ($2\theta = 15\text{--}75^\circ$) for the L6 chondrites: **(a)** A-881806 S1, **(b)** Y-74035 S2, **(c)** Y-793569 S2, **(d)** A-87010 S3, **(e)** Y-86010 S3, **(f)** Y-86007 S3, **(g)** ALH-769 S3, **(h)** A-881091 S3, **(i)** Sahara 98222 S3, **(j)** Mangui S4, **(k)** Y-791771 S4, **(l)** NWA 7984 S4, **(m)** Tenham S5, and **(n)** NWA 4719 S5. **(o)** Bamble powder (orthopyroxene). **(p)** Mpwapwa powder (orthopyroxene). **(q)** Bilanga diogenite powder. **(r)** PDF data of olivine, orthopyroxene, and plagioclase for the present study. Larger closed circles denote focused indices. Red, blue, and green represent olivine, orthopyroxene, and plagioclase, respectively. Olivine (130) at 32.14° , (211) at 41.6° , (222) at 52.0° , and (322) at 69.2° . Orthopyroxene (610) at 31.0° , (511) at 31.5° , (421) at 33.0° , (631) at 46.2° , and (12.1.2) at 72.8° . Plagioclase ($\bar{2}01$) at 22° . The vertical axis shows relative intensity. **(s)** PDF data for other minerals (diopside, kamacite, taenite, and troilite). The vertical axis shows relative intensity.

FIGURE 3. **(a)** Williamson-Hall plot for olivine. Four isolated indices, (130), (211), (222), and (322), are common in the plot. Correlation is mainly 0.7–0.9, regardless of the shock degree. Plot region shifts upward when the shock stage increases, suggesting an increased lattice strain or crystallite size. **(b)** Williamson-Hall plot for orthopyroxene. Five isolated indices, (610), (511), (421), (631), and (12.1.2), are common in the plot. Plot region shifts upward when the shock stage increases, suggesting an increased lattice strain or grain size factor. The closed symbol color was distinguished as black for S1 and S2, red for S3, green for S4, and blue for S5. The symbol shape was distinguished as square A-881806, circle Y-74035, diamond Y-793569, circle A-87010, triangle Y-86010, diamond Y-86007, square ALH-769, inverted triangle A-881091, right triangle

Sahara 98222, circle Y-791771, triangle NWA 7984, hexagon Tenham, and diamond NWA 4719. The symbol color and shape are the same as FIGURES 4, 5, 6, and 9.

FIGURE 4. (a) Relationship for plagioclase ($\bar{2}01$) between FWHM ($^{\circ}$) and integrated intensity. Clockwise rotation is observed as the shock stage increases. Maskelynitization starts from the shock stage more than S4, which is consistent with decreasing intensity in the plot. (b) Relationship between the shock pressure and $I_{Pl(\bar{2}01)}/FWHM_{Pl(\bar{2}01)}$. Peak shock pressure for the shock stage by Stöffler et al. (1991) is also denoted. The symbol color and shape are the same as FIGURE 3.

FIGURE 5. (a) Relationship between $-\log \beta_0^{Ol}$ and $\varepsilon^{Ol}(\%)$ for olivine with 1σ , where β_0^{Ol} is obtained from the β intercept (β at $\tan \theta = 0^{\circ}$) of the Williamson-Hall plot, and $\varepsilon^{Ol}(\%)$ the lattice strain obtained from the slope of the Williamson-Hall plot, ranging from ~ 0.05 – 0.25% . $\varepsilon^{Ol}/-\log \beta_0^{Ol}$ value increases as the shock stage increases. (b) Relationship between $-\log \beta_0^{Opx}$ and $\varepsilon^{Opx}(\%)$ for orthopyroxene with 1σ , where β_0^{Opx} is the β intercept (β at $\tan \theta = 0$) of the Williamson-Hall plot, and $\varepsilon^{Opx}(\%)$ ranges from ~ 0.1 – 0.4% , which is the lattice strain obtained from the slope of the Williamson-Hall plot. $\varepsilon^{Opx}/-\log \beta_0^{Opx}$ value increases as the shock stage increases. The symbol color and shape are the same as FIGURE 3.

FIGURE 6. (a) Shock stage defined by Stöffler et al. (1991) clearly shows a positive correlation with $-\varepsilon^{Ol}/\log \beta_0^{Ol}$ for olivine. Peak shock pressure for the shock stage by Stöffler et al. (1991) is also denoted. (b) Shock stage defined by Stöffler et al. (1991) clearly shows a positive correlation with $-\varepsilon^{Opx}/\log \beta_0^{Opx}$ for orthopyroxene. Peak shock pressure for the shock stage by Stöffler et al. (1991) is also denoted. The symbol color and shape are the same as FIGURE 3.

FIGURE 7. (a) Optical microscope image of the internal texture of shock melt vein in the NWA 4719 L6 chondrite with the shock stage S5. Rwd = ringwoodite. (b) Backscattered electron microscope image of (b). (c) Recrystallized equigranular texture in the NWA 4719 L6 chondrite with the shock stage S5. Ol = olivine (Fa_{25}). Opx = orthopyroxene ($En_{77.7}Fs_{20.8}Wo_{1.5}$). Ca-px = calcium-rich pyroxene ($En_{47}Fs_8Wo_{45}$). Mask = maskelynite ($Ab_{82}An_{11}Or_7$).

FIGURE 8. Raman spectra in the NWA 4719 L6 chondrite. (a) Ringwoodite in shock vein in FIGURE 7a. (b) Maskelynite in equigranular texture in FIGURE 7b in comparison with maskelynite in host lithology, showing the identical spectra.

FIGURE 9. Summary of the present study for reading the shock barometer from the X-ray diffraction data of the three phases of olivine, orthopyroxene, and plagioclase. (a) $\varepsilon^{\text{Ol}} / -\log \beta_0^{\text{Ol}}$ and $I_{Pl(\bar{2}01)} / FWHM_{Pl(\bar{2}01)}$ is given by $-\varepsilon^{\text{Opx}} / \log \beta_0^{\text{Opx}} = -0.01 + 2.0 (-\varepsilon^{\text{Ol}} / \log \beta_0^{\text{Ol}})$ ($R = 0.94$). (b) $I_{Pl(\bar{2}01)} / FWHM_{Pl(\bar{2}01)}$ and $-\varepsilon^{\text{Opx}} / \log \beta_0^{\text{Opx}}$ is given by $-\varepsilon^{\text{Opx}} / \log \beta_0^{\text{Opx}} = 0.25(\pm 0.04) - 8.9 \times 10^{-5} (\pm 2.6 \times 10^{-5}) \times (I / FWHM)_{Pl(\bar{2}01)}$. (c) $I_{Pl(\bar{2}01)} / FWHM_{Pl(\bar{2}01)}$ and $\varepsilon^{\text{Ol}} / -\log \beta_0^{\text{Ol}}$ is given by $-\varepsilon^{\text{Ol}} / \log \beta_0^{\text{Ol}} = 0.14(\pm 0.01) - 5.2 \times 10^{-5} (\pm 5.7 \times 10^{-6}) \times (I / FWHM)_{Pl(\bar{2}01)}$. The symbol color and shape are the same as FIGURE 3.

TABLE 1. Studied L6 chondrites

Sample name	Form	Surface area (cm ²)	Shock stage ^a	Shock stage ^b	This shock stage ^c	Petrography		
						Olivine	Plagioclase	Others
A-881806	PTS(,121-1)	1.8	S1	-	S1	sharp		absent shock vein
Y-74035	PTS(,96-3)	1.0	S1	-	S2	weak undulatory	-	absent shock vein
Y-793569	PTS(,61-1)	1.3	S1	-	S2	weak undulatory	-	absent shock vein
A-87010	PTS(,91-1)	0.8	S3	-	S3	undulatory	-	darkened, absent shock vein
Y-86010	PTS(,51-1)	0.6	S3	-	S3	undulatory	-	absent shock vein
Y-86007	PTS(,51-1)	0.8	S3	-	S3	undulatory	undulatory	a thin shock vein
ALH-769	PTS(,98-2)	2.0	S3	-	S3	undulatory	partial mask	a thin shock vein
A-881091	PTS(,31-1)	1.8	S4	-	S3	PDF, undulatory	-	
Sahara 98222	PTS	1.8	-	S6	S3	weak mosaic	partial mask	shock veins
Manguí	PTS	1.6	-	S5	S4	undulatory	undulatory	a shock vein
Y-791771	PTS(,51-1)	1.3	S4	-	S4	weak mosaic	partial mask	
NWA 7984	PTS	1.6	-	S5	S4	PDF	partial mask	thin shock veins
Tenham	PTS(,51-3)	1.7	S6	-	S5	mosaic	mask	shock vein bearing ringwoodite
NWA 4719	PTS	0.9	S6	S4	S5	mosaic	mask	shock vein bearing ringwoodite

Notes: a = Classification used in Imae et al. (2019); b = Meteoritical Bulletin Database; c = current classification based on the observation of the polished thin sections by the 2nd author; mask = maskelynite; undulatory = undulatory extinction; PDF = planar deformation feature.

TABLE 2. Summary of the analytical results from the Williamson-Hall plot for olivine of the PTSs for the 14 L6 chondrites

Sample	Shock stage	β_0^{O1}	$1\sigma(\beta_0^{O1})$	$1\sigma(\log \beta_0^{O1})$	Slope	$1\sigma(\text{Slope})$	R	ε^{O1}	$1\sigma(\varepsilon^{O1})$	$\varepsilon^{O1}/\log \beta_0^{O1}$	$1\sigma(\varepsilon^{O1}/\log \beta_0^{O1})$
A-881806	S1	0.04	0.01	0.10	0.14	0.02	0.96	0.06	0.01	0.04	0.01
Y-74035	S2	0.09	0.03	0.13	0.14	0.06	0.76	0.06	0.03	0.06	0.03
Y-793569	S2	0.01	0.02	0.41	0.18	0.03	0.94	0.08	0.01	0.04	0.01
A-87010	S3	0.09	0.03	0.11	0.10	0.05	0.68	0.04	0.02	0.04	-
Y-86010	S3	0.05	0.03	0.23	0.29	0.07	0.90	0.13	0.03	0.10	0.03
Y-86007	S3	0.00	0.03	-	0.42	0.07	0.95	0.18	0.03	-	-
ALH-769	S3	0.08	0.04	0.16	0.27	0.07	0.88	0.12	0.03	0.11	0.03
A-881091	S3	0.11	0.02	0.09	0.24	0.05	0.93	0.10	0.02	0.11	0.02
Sahara 98222	S3	0.13	0.01	0.04	0.16	0.03	0.94	0.07	0.01	0.08	0.01
Manguí	S4	0.10	0.06	0.21	0.28	0.13	0.74	0.12	0.05	0.12	0.06
Y-791771	S4	0.02	0.06	0.60	0.51	0.12	0.90	0.22	0.05	0.13	0.06
NWA 7984	S4	0.07	0.04	0.21	0.37	0.09	0.90	0.16	0.04	0.14	0.04
Tenham	S5	0.01	0.03	0.56	0.62	0.06	0.99	0.27	0.02	0.15	0.05
NWA 4719	S5	0.09	0.01	0.05	0.43	0.02	1.00	0.19	0.01	0.18	0.01

TABLE 3. Summary of the analytical results from the Williamson-Hall plot for orthopyroxene of the PTSs for 14 L6 chondrites

Sample	Shock stage	β_0^{Opx}	$1\sigma(\beta_0^{\text{Opx}})$	$1\sigma(\log \beta_0^{\text{Opx}})$	Slope	$1\sigma(\text{Slope})$	R	ε^{Opx}	$1\sigma(\varepsilon^{\text{Opx}})$	$\varepsilon^{\text{Opx}}/\log \beta_0^{\text{Opx}}$	$1\sigma(\varepsilon^{\text{Opx}}/\log \beta_0^{\text{Opx}})$
A-881806	S1	0.06	0.02	0.11	0.20	0.04	0.93	0.09	0.02	0.07	0.02
Y-74035	S2	0.16	0.08	0.18	0.22	0.18	0.78	0.10	0.05	0.12	0.07
Y-793569	S2	0.06	0.13	0.51	0.28	0.31	0.78	0.12	0.13	0.10	0.12
A-87010	S3	0.13	0.03	0.09	0.39	0.07	0.94	0.17	0.03	0.19	0.04
Y-86010	S3	0.03	0.06	0.46	0.48	0.13	0.88	0.21	0.06	0.14	0.06
Y-86007	S3	0.00	0.03	-	0.56	0.06	0.98	0.24	0.03	-	-
ALH-769	S3	0.14	0.05	0.14	0.36	0.12	0.82	0.16	0.05	0.19	0.07
A-881091	S3	0.03	0.10	0.63	0.74	0.22	0.86	0.32	0.10	0.21	0.11
Sahara 98222	S3	0.11	0.06	0.20	0.36	0.15	0.77	0.16	0.06	0.16	0.07
Mangui	S4	-0.02	0.09	-	0.79	0.20	0.89	0.35	0.09	-	-
Y-791771	S4	-	0.01	-	-	0.03	NC ^a	-	-	-	-
NWA 7984	S4	0.06	0.32	0.80	0.91	0.72	0.86	0.40	0.31	0.32	0.32
Tenham	S5	0.10	0.07	0.22	0.68	0.15	0.92	0.30	0.07	0.29	0.09
NWA 4719	S5	-	0.01	-	-	0.03	NC ^a	-	-	-	-

Note: a = No correlation.

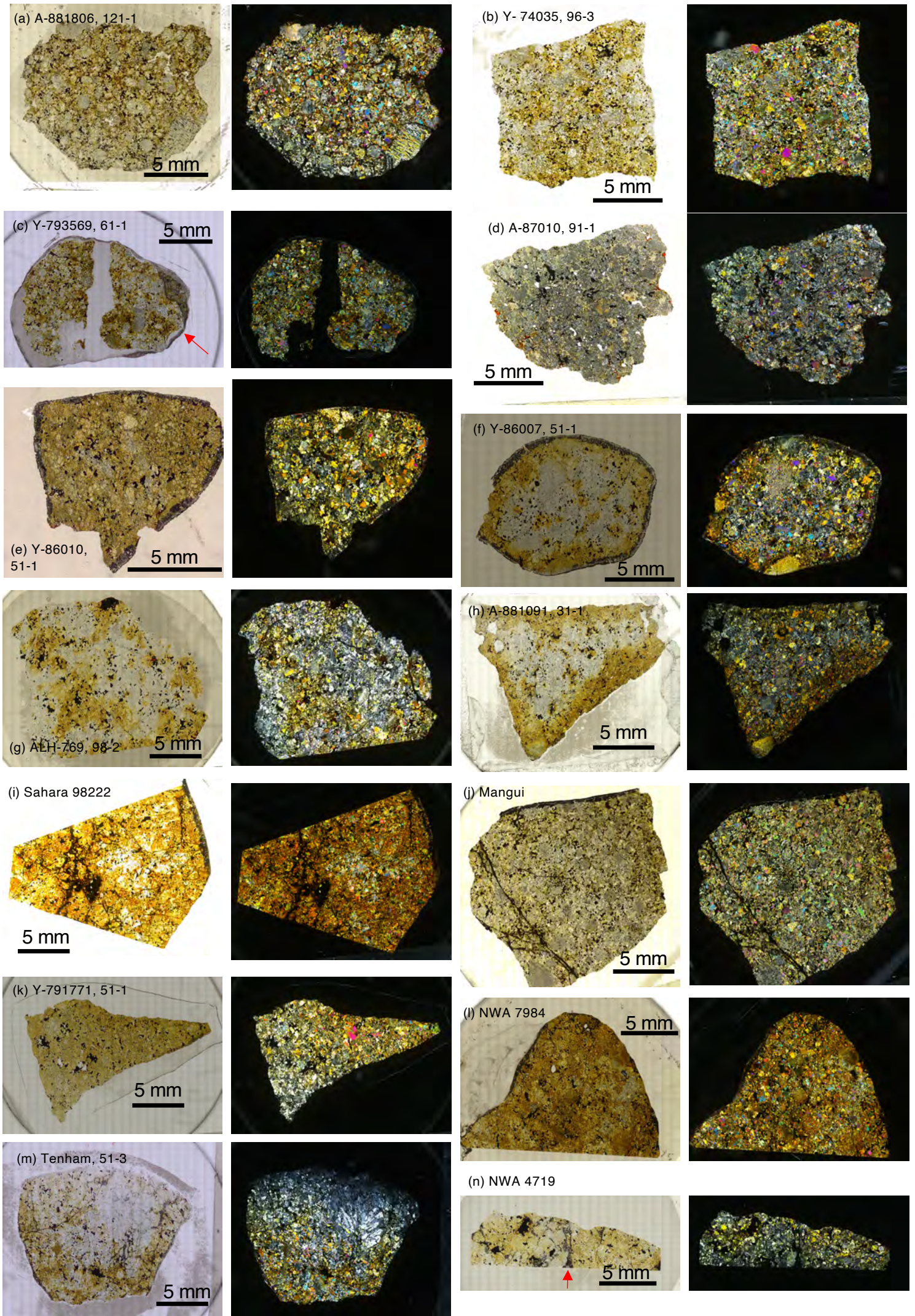


FIGURE 2

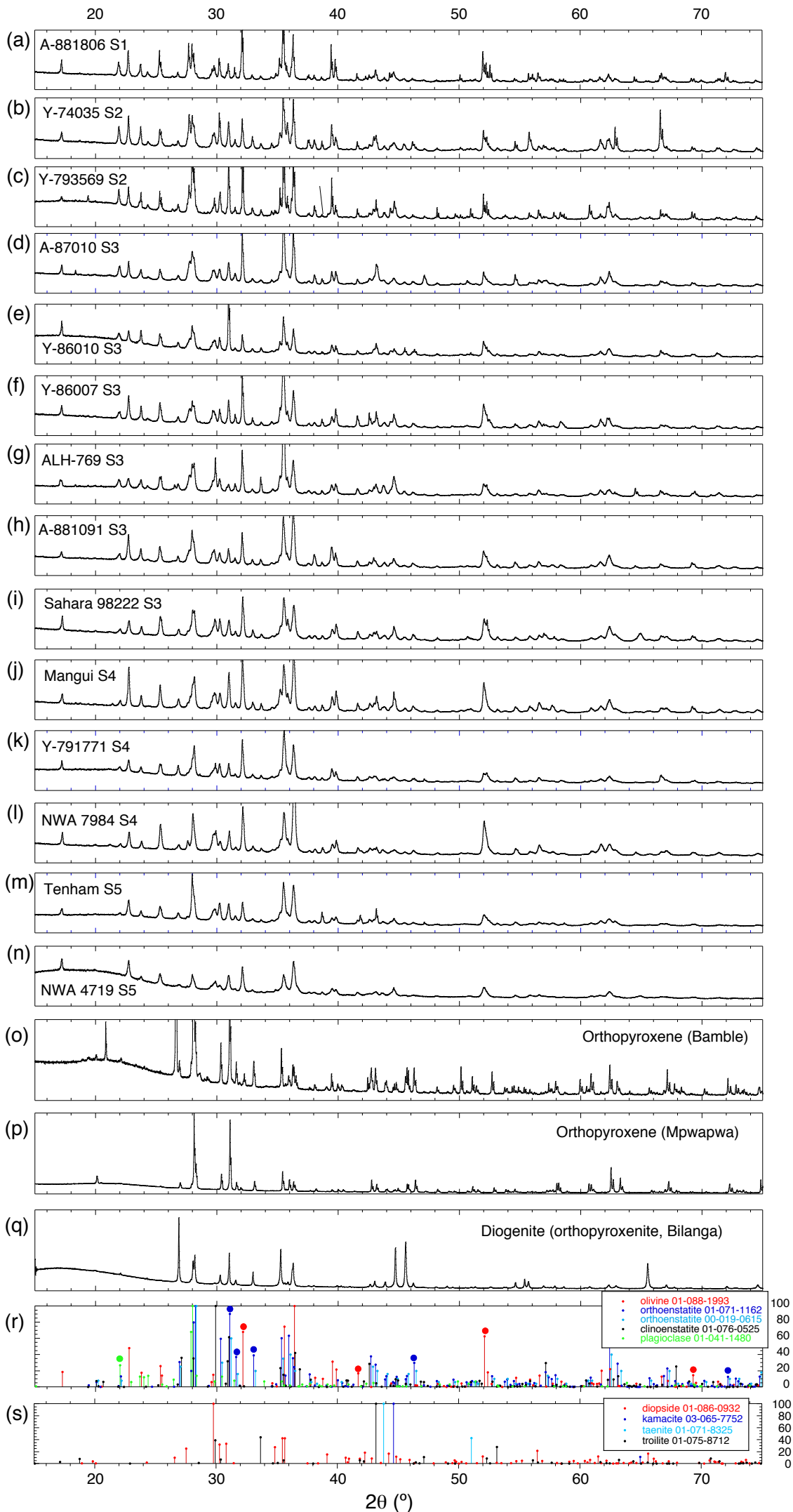
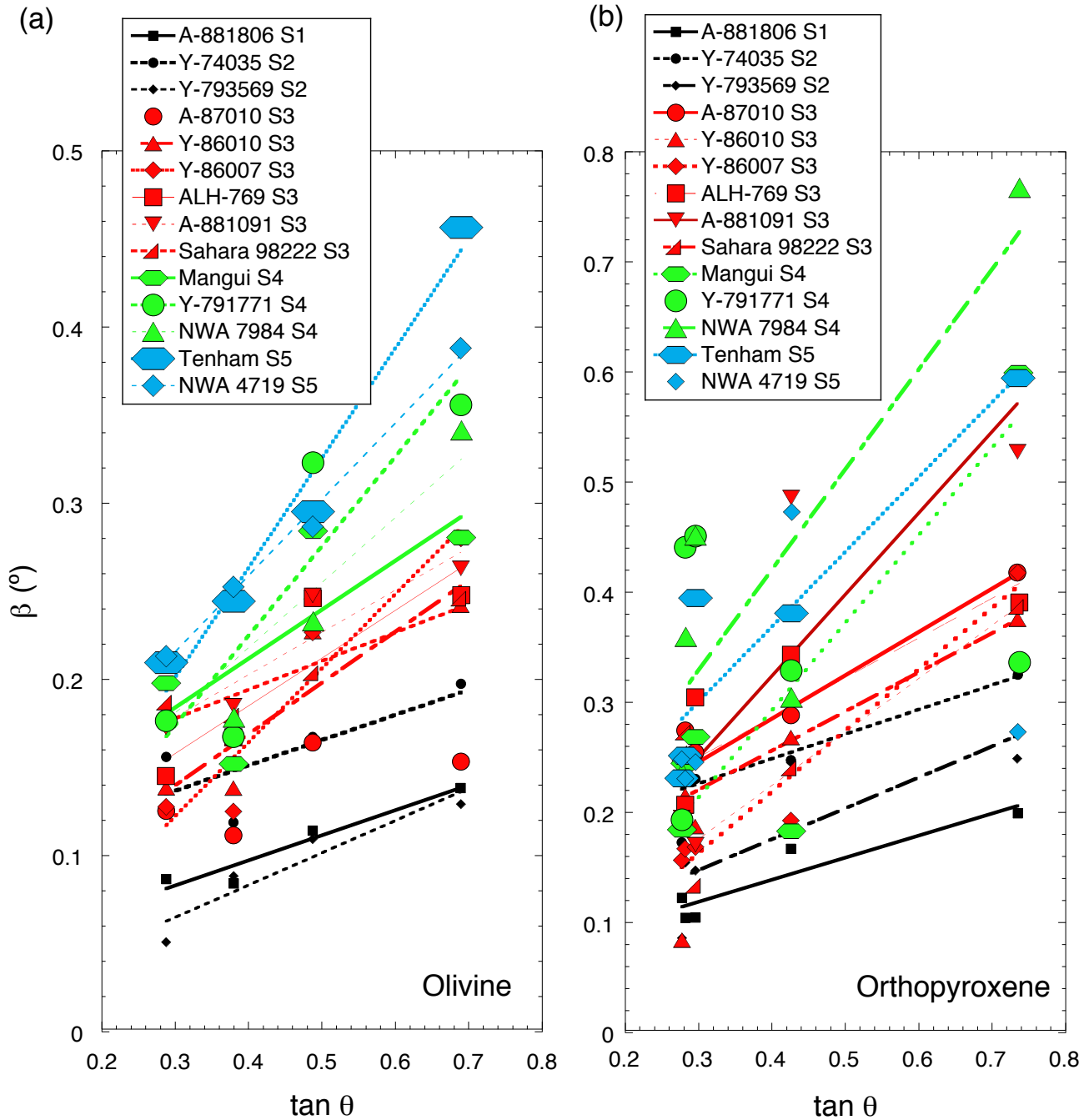
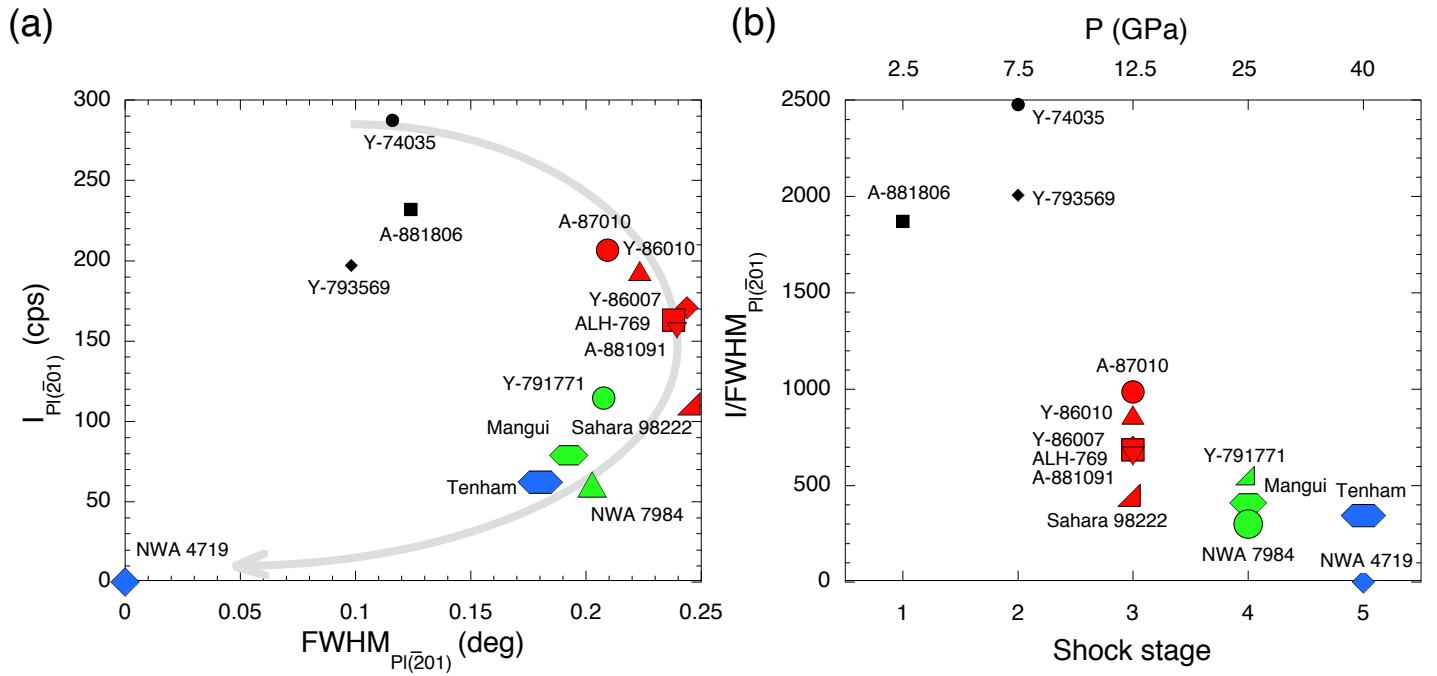
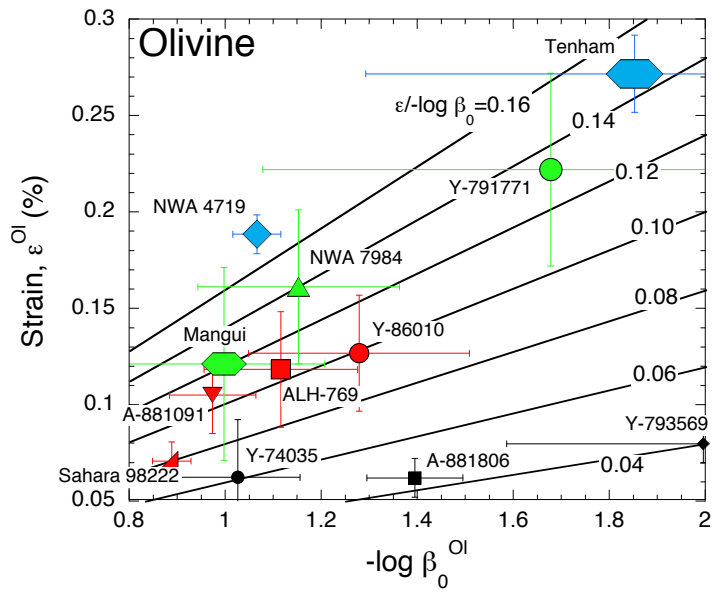


FIGURE 3

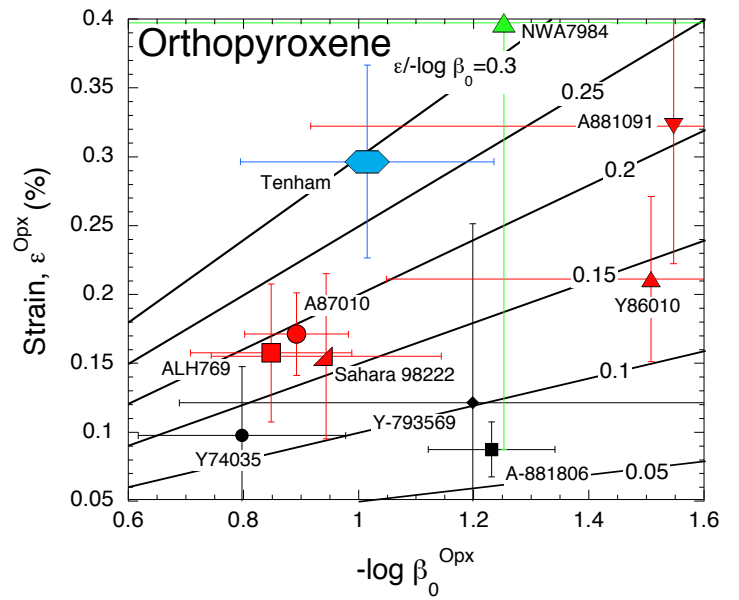




(a)



(b)



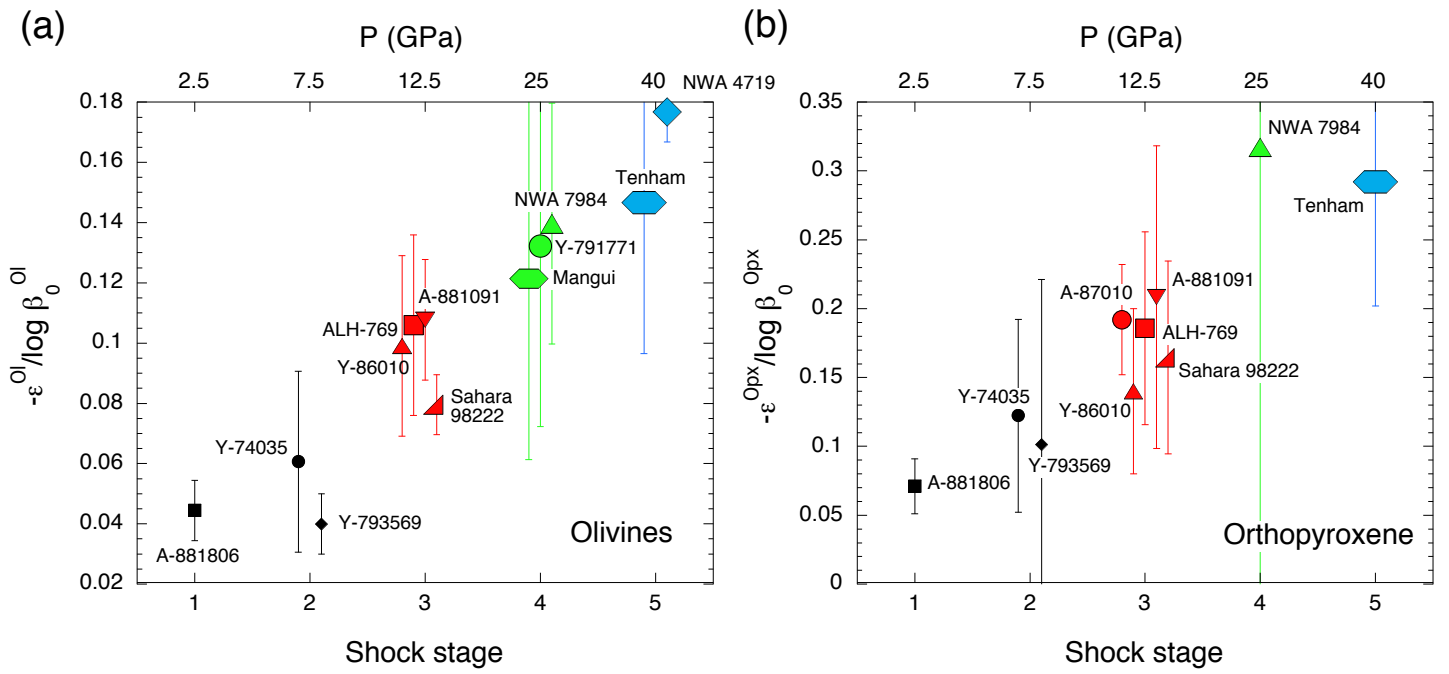
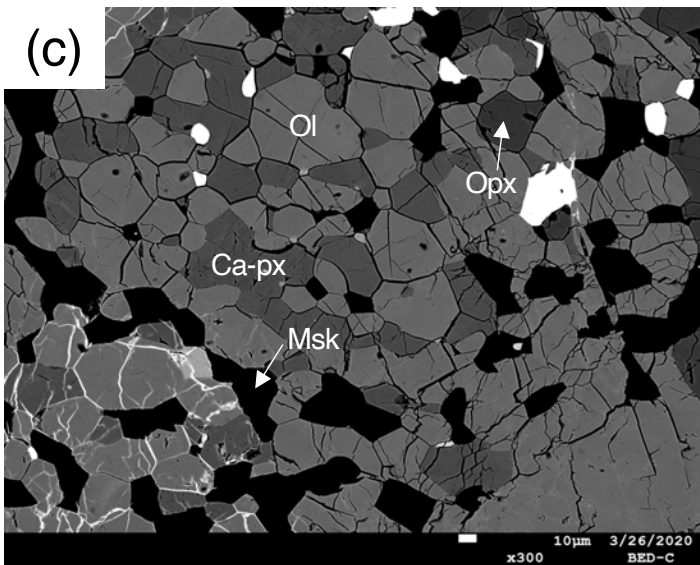
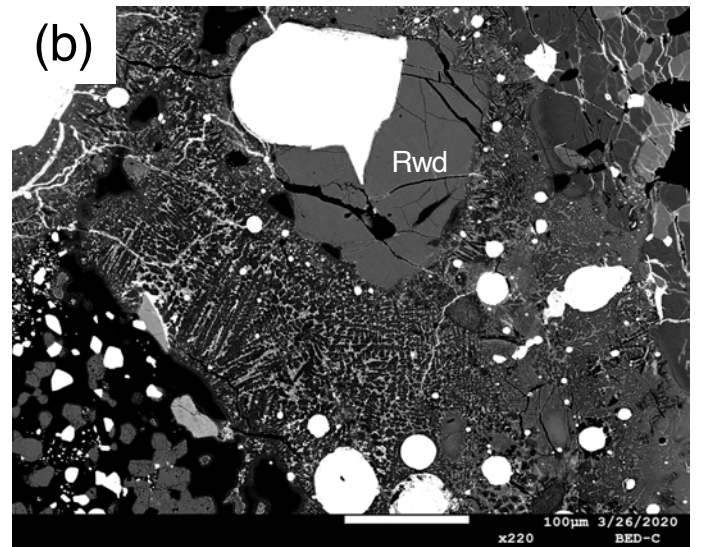
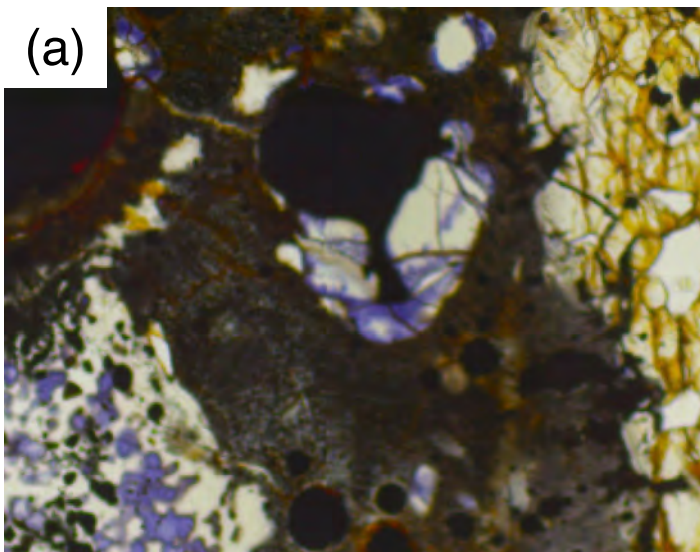
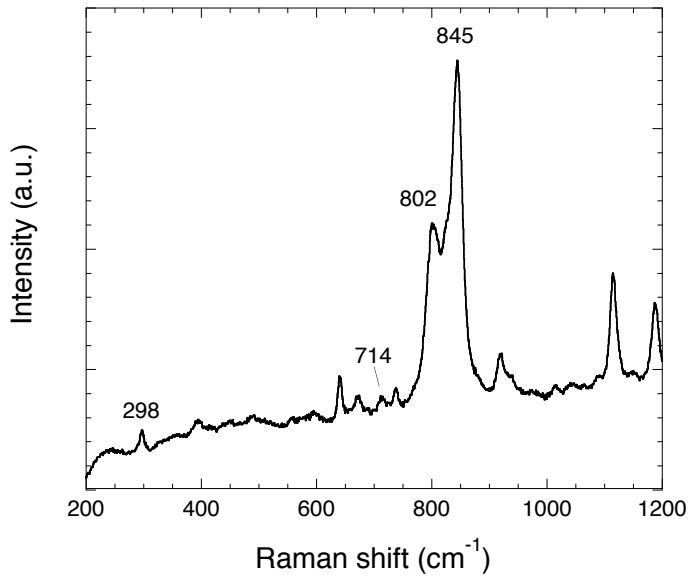


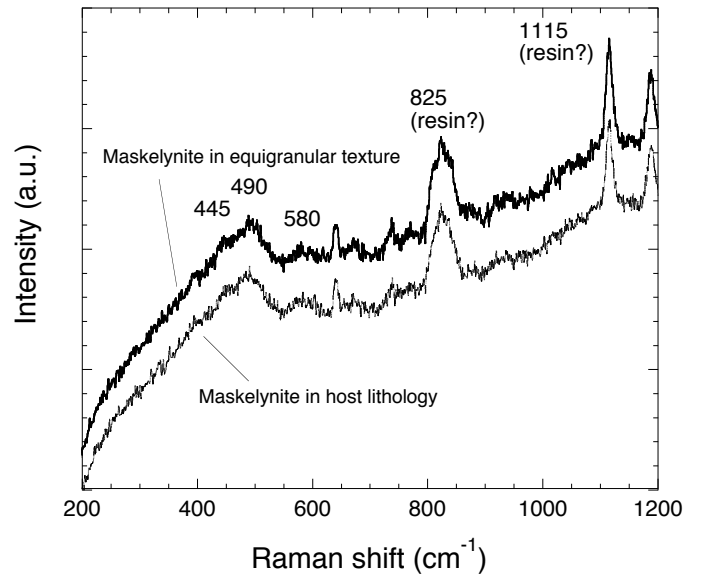
FIGURE 7



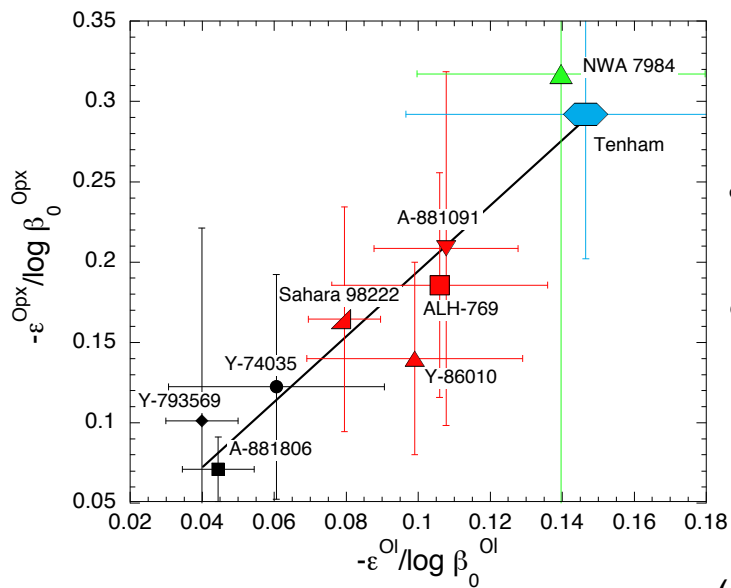
(a)



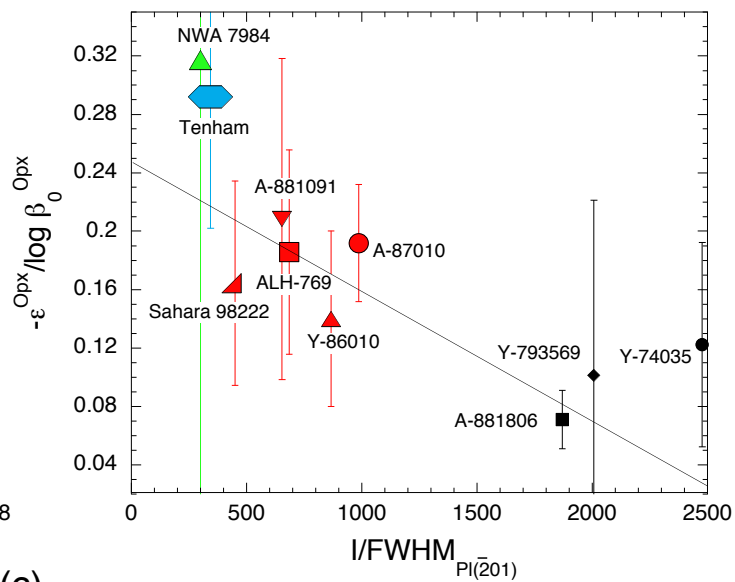
(b)



(a)



(b)



(c)

